Earth and Space Science

RESEARCH ARTICLE
10.1029/2020EA001219

Deep Learning Models for Estimation of the SuperDARN Cross Polar Cap Potential

Erxiao Liu[1,2], Hongqiao Hu[3], Jianjun Liu[3], and Lei Qiao[1]

[1]School of Communication Engineering, Hangzhou Dianzi University, Hangzhou, China, [2]Department of Electrical and Computer Engineering, Virginia Tech, Blacksburg, VA, USA, [3]State Oceanic Administration Key Laboratory for Polar Science, Polar Research Institute of China, Shanghai, China

Key Points:
- SuperDARN CPCP models by applying deep learning techniques are developed
- The models take near-Earth parameters and their history measurements as input vectors producing lower RMSE and higher LC than other models
- The deep learning models accurately captures the CPCP nonlinear properties

Correspondence to:
E. Liu,
liuerxiao@hdu.edu.cn

Citation:
Liu, E., Hu, H., Liu, J., & Qiao, L. (2020). Deep learning models for estimation of the SuperDARN cross polar cap potential. *Earth and Space Science*, *7*, e2020EA001219. https://doi.org/10.1029/2020EA001219

Received 14 APR 2020
Accepted 16 JUL 2020
Accepted article online 5 AUG 2020

Abstract We present deep learning models for cross polar cap potential (CPCP) by applying multilayer perceptron (MLP) and long short-term memory (LSTM) networks to estimate CPCP based on Super Dual Auroral Radar Network (SuperDARN) measurements. Three statistical parameters are proposed, which are root-mean-square error (RMSE), mean absolute error and linear correlation coefficient (LC), to validate and test the models by measuring their performance on an independent data set that was withheld from the training data set. In addition, we compare the models with previous work. The results show that the deep learning models can successfully reproduce the CPCP values with much lower RMSE (8.41 kV for MLP and 7.20 kV for LSTM) and mean absolute error (7.22 kV for MLP and 6.28 kV for LSTM) and higher LC (0.84 for MLP and 0.90 for LSTM) than do the other models, which have RMSE larger than 10 kV and LC lower than 0.75. The deep learning models can also express the CPCP nonlinear properties (saturation effect) accurately. This study demonstrates that deep learning techniques can enhance the ability to predict CPCP.

1. Introduction

It is generally believed that there are two types of mechanisms whereby energy and momentum are input into the magnetosphere-ionosphere system from the solar wind. The primary one is the process of magnetic merging on the dayside of the magnetopause with the interplanetary magnetic field (IMF) (Dungey, 1961), and the secondary one is a viscous-like interaction, which is generally thought to couple energy from the solar wind into the magnetosphere at a rate smaller than that of reconnection (Axford & Hines, 1961; Cowley & Lockwood, 1992). The plasma convection in the magnetosphere arising from these two processes maps along almost equipotential geomagnetic field lines with little attenuation into the high-latitude ionosphere, resulting in ionospheric plasma convection and an associated polar electric potential variation. The total electrostatic potential variation across the polar region, referred to as the cross polar cap potential (CPCP), is thus a critical indicator of the energy flow into the coupled magnetosphere-ionosphere system (Adhikari et al., 2017).

Numerous studies have been undertaken to measure the CPCP and to determine the relationship of the CPCP to solar wind drivers and other geophysical parameters using a variety of observations and techniques, including measurements from satellites (Boyle et al., 1997; Doyle & Burke, 1983; Förster & Haaland, 2015; Hairston et al., 2005; Reiff et al., 1981; Russell et al., 2001; Weimer, 1996, 2005), ground-based magnetometers (Ridley, 2005; Ridley et al., 2000), and incoherent radars (Clauer et al., 2016; Zhang et al., 2007). A new era in ionospheric convection and CPCP studies began owing to the introduction of the Super Dual Auroral Radar Network (SuperDARN) coherent radar network from the end of the twentieth century for measurements of the CPCP directly (Gillies et al., 2011; Grocott et al., 2017; Kustov et al., 1997; Liu et al., 2019; Ruohoniemi & Baker, 1998; Ruohoniemi & Greenwald, 1996, 2005; Shepherd, 2007; Thomas & Shepherd, 2018; Wilder et al., 2011). In these previous studies, the interplanetary electric field (IEF), the Kan-Lee merging electric field (Ekl) proposed by Kan and Lee (1979), the Alfven Mach number (*Ma*), the polar cap index (PCN in the Northern Hemisphere), and the *AE* and *Kp* indices have all been proposed to study the relationships between the solar wind, magnetosphere, and ionosphere. Shepherd et al. (2002) studied the relationships between the solar wind, IMF conditions, and the CPCP derived from 2-min SuperDARN high-frequency (HF) backscatter observations during 1998–2000 and showed a clear nonlinear response of the CPCP on the merging electric field. A more focused study of the CPCP dependence on IMF

and solar wind conditions was performed by Shepherd et al. (2003), who found a saturation effect in the CPCP starting from 2 to 5 mV/m in the Ekl and the dependence on the solar wind pressure is not clear. Saturation of the CPCP was also articulated in data by Hairston et al. (2003), who presented clear evidence of a nonlinear response of the CPCP consistent with model predictions by Bristow et al. (2004) and a later paper by Khachikjan et al. (2008), but contrasting with Boyle et al. (1997), who insisted that there was no evidence of saturation of the polar cap potential for large IMF. Many other studies have been implemented in empirical models to predict or model the CPCP and also demonstrated that the CPCP responds to the IEF linearly at low and moderate values but becomes saturated at large values (Shepherd, 2007). However, there is disagreement regarding the threshold IEF value from which nonlinearity begins. While some studies (Khachikjan et al., 2008; Koustov et al., 2009; Russell et al., 2001) identified it as ~3 mV/m, Liemohn and Ridley (2002) argued that it is actually as large as 10 mV/m.

The work presented in this paper concentrates on proposing new prediction models for the CPCP using deep learning techniques based on SuperDARN data. Deep learning techniques have been proven to be powerful tools for nonlinear prediction that accounts for the history of the input parameters (Lin et al., 2018; Wang, 2016). They have been applied to space weather for prediction and to modeling of solar and geomagnetic activities or relevant parameters, such as prediction of solar wind velocity (Wintoft & Lundstedt, 1999), prediction of energetic solar particle events (Hoff et al., 2003), prediction of solar flares (Borda et al., 2002), prediction of geomagnetic indices (Tan et al., 2018; Valach et al., 2009), and total electron content forecasting (Sun et al., 2017). In this study, deep learning techniques are exploited to build models of the CPCP. Several techniques are implemented to improve the accuracy of prediction using these models. Initially, to mitigate the low efficiency and overfitting of the deep learning algorithms on account of redundant and irrelevant features, we select parameters with the highest correlation coefficients to make the models as efficient as possible. This helps the models to determine input matrices that have high correlations for the prediction process. This technique could bring better performance for prediction models when dealing with multivariate data. Second, the historical values of parameters are used to further improve the prediction performance because the current CPCP value not only is associated with the current solar wind, magnetosphere, and geomagnetic conditions but also is constrained by their recent histories (Bristow et al., 2004). Finally, the multilayer perceptron (MLP) neural network and long short-term memory (LSTM) techniques are employed to predict the CPCP. In order to evaluate the effectiveness of the proposed models, we carry out testing with a different data set. The results demonstrate the feasibility of our approach for multivariate CPCP prediction with high efficiency.

2. Methods and Data Sets

2.1. MLP Neural Network and LSTM Algorithms

A MLP neural network functions like a biological neural network and is an interconnected assembly of simple processing elements, units, or neurons that is based on the neural configuration of the brain. MLP can handle large data sets and has the ability to capture nonlinear and complex underlying relationships of any physical process with plenty of data (Yang, Shen, et al., 2018). The architectural design of a neural network in this study consists of five layers: an input layer, three hidden layers, and an output layer. Each of these layers is made up of nodes or neurons that are information processing units.

LSTM developing from recurrent neural networks is able to store and access information over long periods of time (Graves, 2012; Yang, Zheng, et al., 2018). The ordinary node of the hidden layer is replaced with a memory cell. The LSTM network is governed by the following set of equations, and all of the elements of the memory cell are described below.

$$i_t = \sigma\left(\sum_{k=1}^{30} w_{ihk} h(t-k) + w_{ix} \cdot x(t-1) + b_i\right)$$

$$f_t = \sigma\left(\sum_{k=1}^{30} w_{fhk} h(t-k) + w_{fx} \cdot x(t-1) + b_f\right)$$

$$O_t = \sigma\left(\sum_{k=1}^{30} w_{ohk} h(t-k) + w_{ox} \cdot x(t-1) + b_o\right)$$

$$C(t) = C(t-1)\otimes f_t + i_t \otimes \tanh\left(\sum_{k=1}^{30} w_{chk} h(t-k) + w_{cx} \cdot x(t-1) + b_c\right)$$

$$h_t = O_t \otimes \tanh(C(t))$$

where i_t, f_t, O_t, and $C(t)$ represent the outputs of the input gate, the forget gate, the output gate, and the cell state, respectively; h_t is the final cell output; and σ is a sigmoid function with a value between 0 and 1. w_{ihk}, w_{ix}, w_{fhk}, w_{fx}, w_{chk}, w_{cx}, w_{ohk}, and w_{ox} are the weight factor matrix for the input gate, the forget gate, the cell state, and the output gate, respectively. b_i, b_f, b_c, and b_o are the bias terms for these gates. $\otimes$ represents the element-wise Hadamard product. Using all of these parameters, the LSTM algorithm can explain the relationship between current values and their history information, and considering that the CPCP may be affected by not only the simultaneous values of near-Earth space parameters but also their history, we proposed the LSTM algorithm to predict the CPCP in this study.

2.2. Data Sets and Data Preprocessing

2.2.1. SuperDARN Data Set

SuperDARN is an international network consisting of chains of ground-based HF radars that monitor ionospheric plasma convection from the middle to high latitudes in both hemispheres (Chisham et al., 2007; Huang et al., 2018; Nishitani et al., 2019). The instantaneous ionospheric convection pattern can be derived from SuperDARN using the map potential fitting technique by combining line-of-sight velocity measurements (Ruohoniemi & Baker, 1998; Shepherd & Ruohoniemi, 2000). In the technique, the fitting is done by first representing the electrostatic potential on a shell by a series expansion in terms of spherical harmonic basis functions, and then the electric potential can be determined at any point in the mapping region if the SuperDARN radars are performing their measurements. In this procedure, the instantaneous line-of-sight vectors are supplemented with model data sampled from the appropriate statistical pattern of Ruohoniemi and Greenwald (1996) (hereafter referred to as RG96) determined as a function of IMF B_y and B_z in regions where instantaneous data are unavailable, preventing the solution from becoming unphysical. Then, the difference of potential between the minimum on the dusk side and maximum on the dawn side of the convection is defined as CPCP. Thomas and Shepherd (2018) derived a statistical model of ionospheric convection using velocity measurements from the complete SuperDARN network of midlatitude, high-latitude, and polar cap radars (hereafter referred to as the TS18 model), which can increase the measured CPCP by as much as 40% for strong solar wind driving. In this work, the CPCP values are from the ionospheric convection map based on the TS18 model, and the data from RG96 are also used for comparison. Two-minute data sets are considered in this study. Figure 1 shows the distribution of SuperDARN radars in the Northern Hemisphere and a typical ionospheric convection pattern obtained by the map potential technique for 1946–1948 UT on 16 April 2015.

The CPCP data sets are collected from 2015, one part of which is used for training and the other part of which is used for testing. In this study, we follow the selection criteria of Mori and Koustov (2013), who selected CPCP data obtained with radar coverage of >300 points. Maps with small numbers of echo points are poorly constrained and tend to mimic the statistical model. In this work, we choose the potential maps with echo numbers larger than 300. Accordingly, a total of 66,335 samples is selected, 39,801 of which are training data and 26,534 of which are testing data. Histograms of CPCP data used in this study are shown in Figure 2. The CPCP values mainly range from 15 to 110 kV, while the number of echo vectors for most patterns are larger than 350. The distributions for the training and testing data sets are quite similar, thus reducing the influence of data imbalance between the training and testing processes.

2.2.2. Input Data Source

Deciding the parameters to use as inputs for the deep learning training is important in order to obtain an effective network. We initially chose the widely used parameters, which are IEF, Ekl, PCN, *AE*, *Ma*, and the standoff distance to the magnetopause (R_{ms}). One-minute-resolution OMNI data are obtained from the National Aeronautics and Space Administration Goddard Space Flight Center/Space Physics Data Facility OMNI website and averaged over 2 min. The OMNI data set uses multispacecraft measurements of the interplanetary parameters that are lagged to the subsolar point on the Earth's bow shock. The correlation coefficients of these potential parameters with CPCP are shown in Figure 3. The figure tells us that at the same lag moment, different parameters have different correlations with CPCP. IEF, Ekl, and the *AE* index

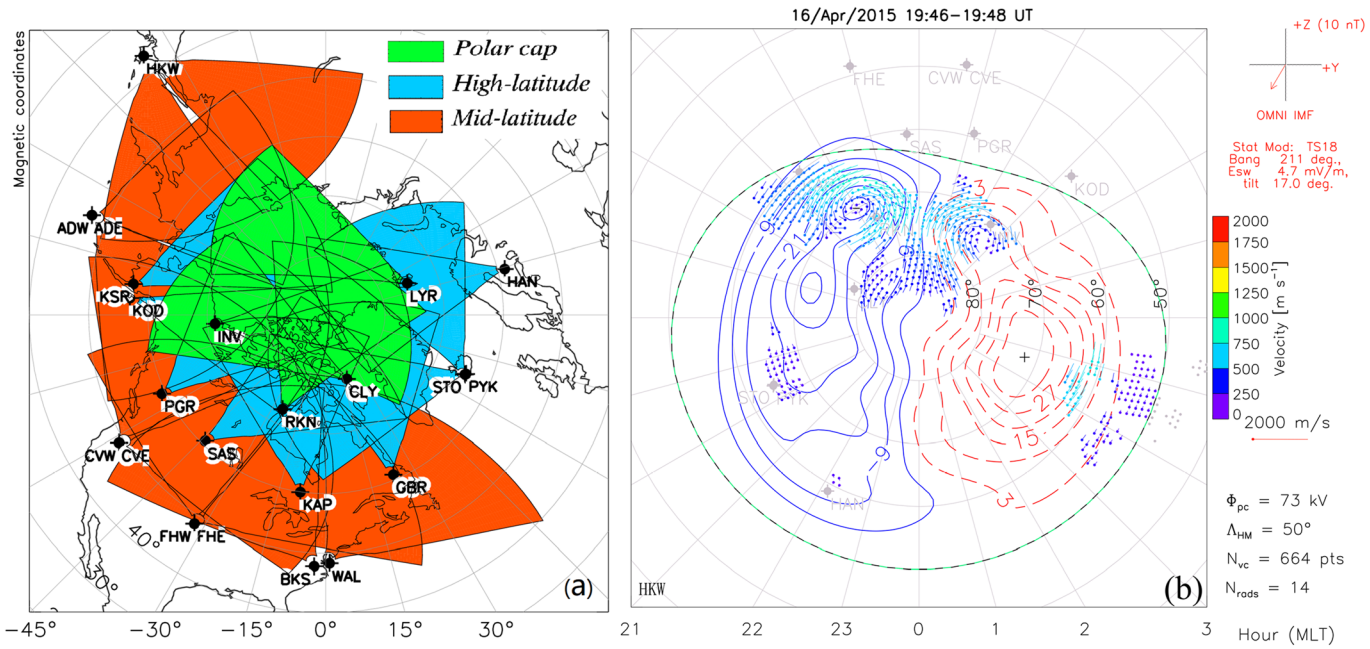

Figure 1. (a) Distribution of SuperDARN radars in the Northern Hemisphere and (b) a typical SuperDARN convection map for 1946–1948 UT on 16 April 2015. The CPCP is the electric potential difference between the maximum (plus sign) and the minimum (minus sign). The CPCP in this pattern is 73 kV.

are highly correlated with CPCP among the parameters, with coefficients of 0.68, 0.74, and 0.65, respectively, at 0 lag. PCN, R_{ms}, and *Ma* are moderately correlated with CPCP with smaller coefficients. The correlation drops with increasing lag time. We use three typical statistical parameters, the root-mean-square error (RMSE), mean absolute error (MAE), and linear correlation coefficients (LC), between observations and predictions to evaluate the prediction accuracy as follows:

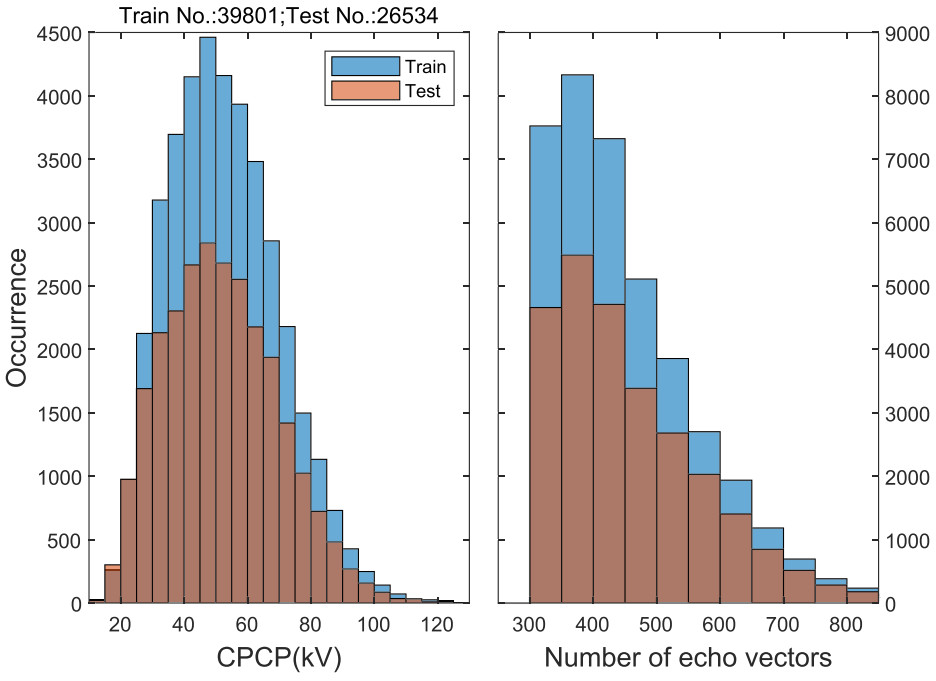

Figure 2. Histograms of CPCP and number of echo vectors for training and testing data sets. A total of 39,801 and 26,534 samples are selected for training and testing, respectively.

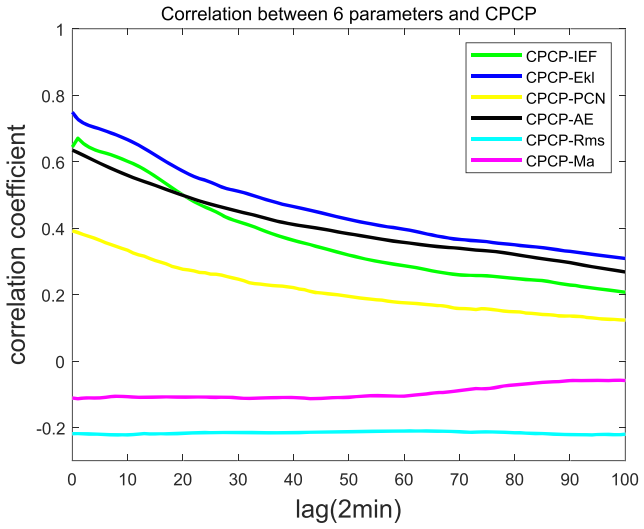

Figure 3. The correlation coefficient dependence on lags for CPCP and different parameters.

$$\mathrm{RMSE} = \sqrt{\frac{\sum_{i=1}^{N}\left(\mathrm{cpcp}_i^{\mathrm{SD}} - \mathrm{cpcp}_i^{\mathrm{model}}\right)^2}{N}}$$

$$\mathrm{MAE} = \frac{\sum_{i=1}^{N}\left|\mathrm{cpcp}_i^{SD} - \mathrm{cpcp}_i^{\mathrm{model}}\right|}{N}$$

$$\mathrm{LC} = \frac{\sum_{i=1}^{N}\left(\mathrm{cpcp}_i^{SD} - \overline{\mathrm{cpcp}^{SD}}\right)\left(\mathrm{cpcp}_i^{\mathrm{model}} - \overline{\mathrm{cpcp}^{\mathrm{model}}}\right)}{\sqrt{\sum_{i=1}^{N}\left(\mathrm{cpcp}_i^{SD} - \overline{\mathrm{cpcp}^{SD}}\right)^2}\sqrt{\sum_{i=1}^{N}\left(\mathrm{cpcp}_i^{\mathrm{model}} - \overline{\mathrm{cpcp}^{\mathrm{model}}}\right)^2}}$$

Since the potential may depend not only on the instantaneous value of the solar wind/IMF parameters but also on their history values, which may provide unique useful constraining information on CPCP prediction, we discuss the effect of different combinations of these parameters, which can be easily realized in MLP and LSTM. Overall, the combinations used here are the following ones, which are noted as D1 (IEF); D2 (Ekl); D3 (*AE*); D4 (IEF and Ekl); D5 (IEF and *AE*); D6 (Ekl and *AE*); D7 (IEF, Ekl, and *AE*); D8 (IEF, Ekl, *AE*, PCN, and *Ma*); D9 (IEF, Ekl, *AE*, PCN, *Ma*, and R_{ms}); D10 (IEF, Ekl, *AE*, and their 4-min historical values); D11 (IEF, Ekl, *AE*, and their 8-min historical values); D12 (IEF, Ekl, *AE*, and their 12-min historical values); D13 (IEF, Ekl, *AE*, and their 16-min historical values); and D14 (IEF, Ekl, *AE*, and their 20-min historical values). We test MLP and LSTM using these different input parameters and evaluate how their performances vary with change of inputs. The results are shown in Figure 4. The MLP and LSTM performances vary with different input combinations and improve with the addition of more parameters until D7, which is composed of IEF, Ekl and *AE*, but the performance might go down when still more parameters are

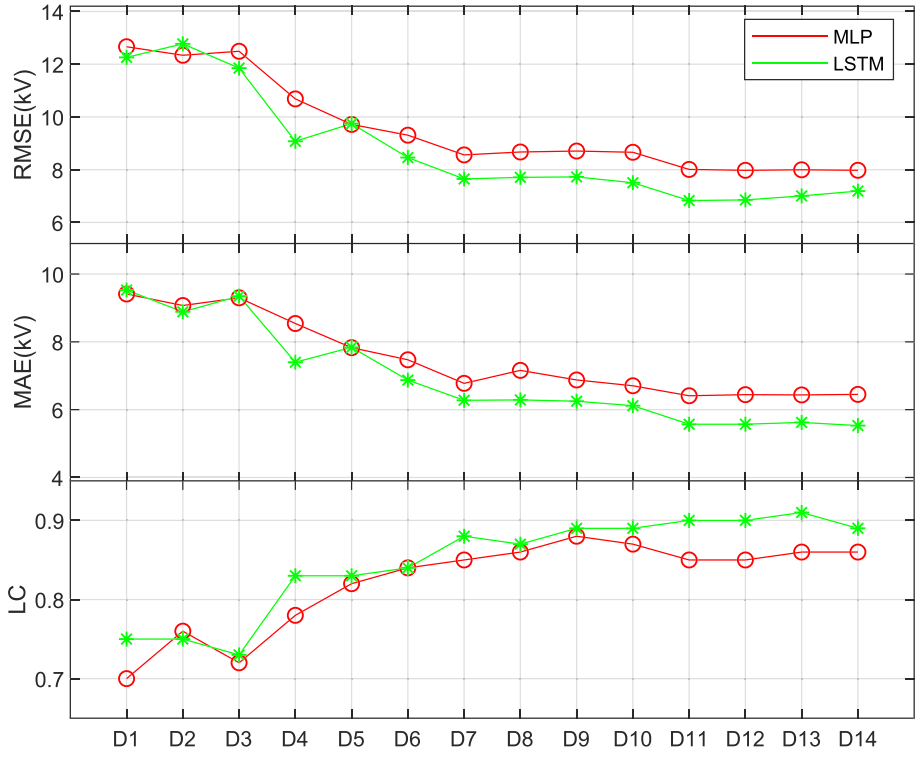

Figure 4. The performances of MLP and LSTM with different combinations of parameters as input based on the training data set.

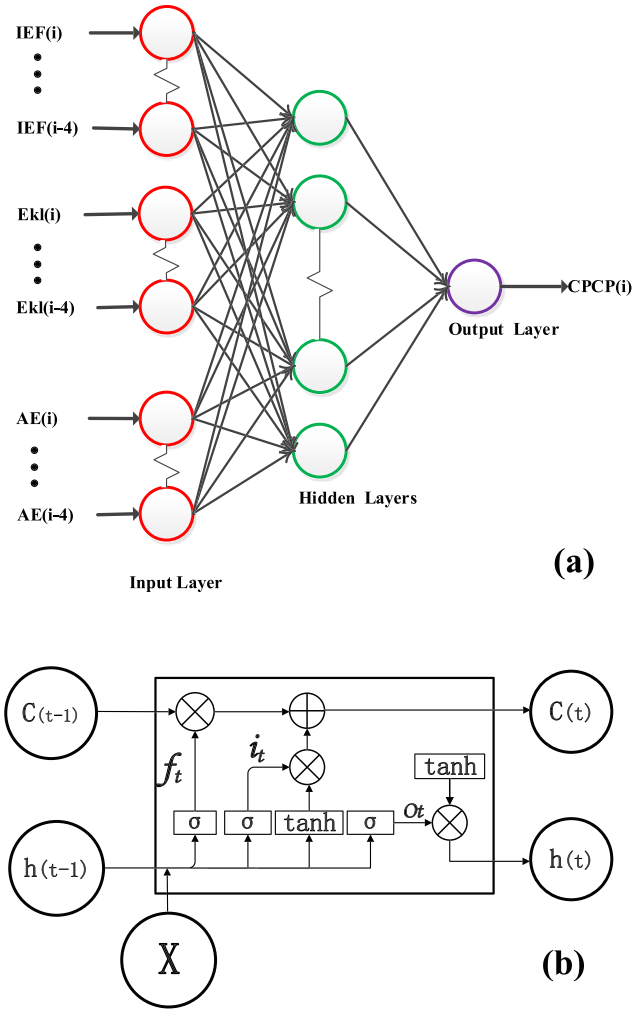

Figure 5. (a) MLP neural network and (b) LSTM network architecture used in this study.

included. Consequently, the addition of PCN, R_{ms}, and *Ma* are not necessary to improve the performance. With D10, the different time span historical values of IEF, Ekl, and *AE* are included, and an obvious better performance is realized with D11, which includes 8-min historical values. After that, the performance no longer improves.

Considering the above conclusions and the possible influences of solar and geomagnetic activities on CPCP, we use IEF, Ekl, the *AE* index, and their 8-min historical values to compose the input vectors to the MLP and LSTM network, whose geometric architectures are presented in Figure 5. In Figure 5b, the X symbol is a matrix composed of IEF, Ekl, *AE*, and their historical values.

3. Performance Comparison

In order to examine the extent to which the deep learning techniques can make predictions, we evaluate the MLP and LSTM models in three aspects. First, we compare the curves of predictions and observations to analyze their learning ability, then we give the error histograms for the training and testing data sets, and at last, we calculate RMSE, MAE, and LC between observation and prediction to present the model ability quantitatively.

Figure 6 displays the predicted (green line for MLP and blue line for LSTM) and measured (red line) values of CPCP for two selected time intervals. The lines show a fairly good match between the predicted and observed values at first glance of the figure. Further visual examination gives the impression that the trained MLP and LSTM networks predict the measured CPCP quite well, including sudden increases or decreases. For example, for the interval 0000–0600 UT on 11 January 2015, several remarkable fluctuations occur for CPCP, and MLP and LSTM capture these changes successfully. When we zoom into the figure and look at the curves more carefully, we still find the CPCP variations from the deep learning techniques matching well with the measurements.

The $\Delta\text{CPCP} = \text{CPCP}_{\text{SD}} - \text{CPCP}_{\text{model}}$ histogram distributions are presented in Figure 7: Figures 7a and 7b are for the training data, while Figures 7c and 7d are for the testing data. The red solid curves are Gaussian best estimates with the mean (μ) and variance (σ) values shown in the upper left corner. Visually, the error ΔCPCP mostly obeys a normal distribution. For training data, the distribution for MLP has a mean value of −0.47 with a variance of 7.279 kV, while the LSTM result has a mean value of −0.27 and a little smaller variance of about 6.353 kV. For testing data, the mean values are −0.79 and −0.357, while the variances are 8.117 and 6.337 kV for MLP and LSTM, respectively. The results of the LSTM model are somewhat more concentrated with a narrow distribution centered on a value a little smaller than the MLP value. The number of the peak value from LSTM is slightly larger than that from the MLP model, which indicates that LSTM is a little better at CPCP forecasting than MLP.

Further specific testing of the predictions and measurements is summarized in Figure 8. The red dashed line represents the ideal case when the prediction is equal to the measured CPCP. Contours of data occurrence are plotted at the top. A quick view tells us that the results are quite similar between MLP and LSTM. The values of the correlation coefficients obtained between SuperDARN measurements and corresponding deep learning predictions are greater than 0.84 for all cases. This is an indication that the model predictions correlate well with the measurements. The RMSE values computed are, respectively, 7.26 and 6.35 kV for the MLP and LSTM models using training data, while they are 8.41 and 7.20 kV using testing data. The bigger LC and smaller RMSE for LSTM compared to those for the MLP model further indicates a slightly better prediction performance for the LSTM model. The MAE values from the two models are consistent with the

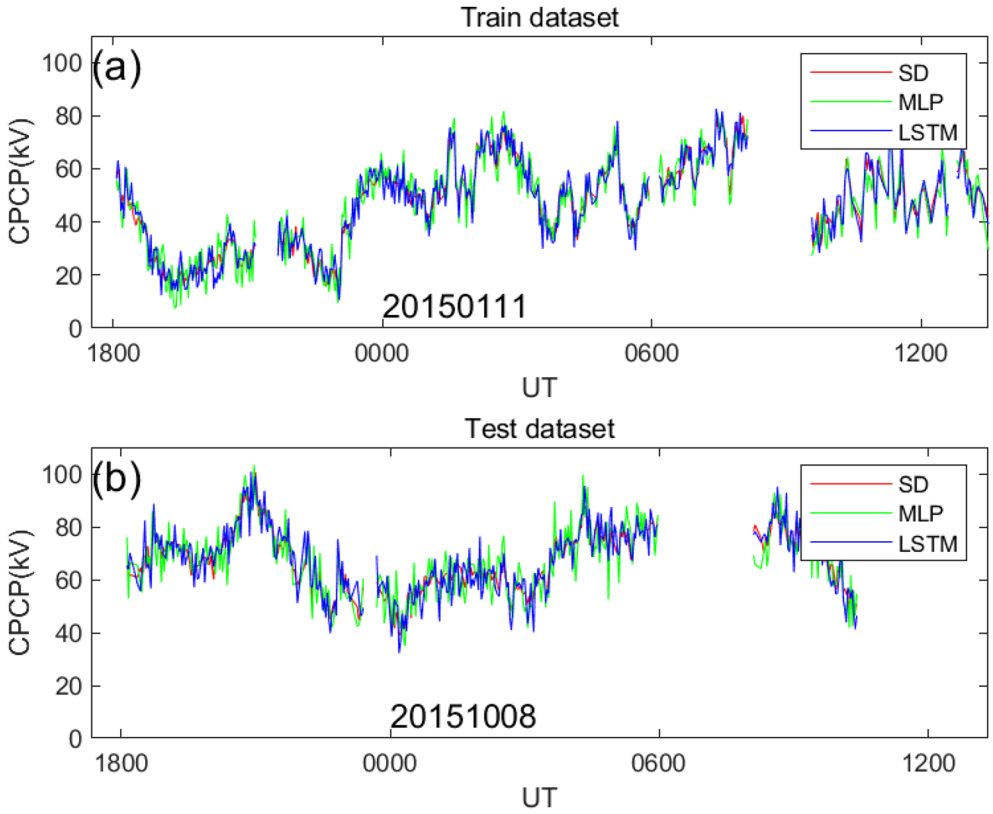

Figure 6. UT variations of the CPCP for two example days in the (a) training data set and (b) testing data set.

RMSE with lower values of 5.06 kV (training) and 6.28 kV (testing) for LSTM compared to 5.80 kV (training) and 7.22 kV (testing) for MLP. The LSTM model in forecasting the CPCP has the smallest RMSE and MAE and largest LC for both the training data set and the testing data set.

4. Discussion

We all know that it is not easy to estimate or predict the CPCP values with high accuracy whether from measurements provided by satellite-based or ground-based equipment or from analytical models. Even so, many important studies have been devoted to this task. Boyle et al. (1997) derived an empirical analytical model of the CPCP from Defense Meteorological Satellite Program satellite data, which has the functional form:

$$\mathrm{CPCP} = 10^{-4}v^2 + 11.7B\sin^3(\theta/2) \tag{1}$$

where v is the solar wind velocity in kilometers per second, B is the magnitude of the IMF and $\theta = \cos^{-1}(B_z/B)_{\mathrm{GSM}}$. This work was improved on by Ridley (2005), who better specified the CPCP by taking into account the size of the magnetosphere and the solar wind Mach number and obtained it as

$$\mathrm{CPCP} = (10^{-4}v^2 + 11.7B\left(1 - e^{-Ma/3}\right)\sin^3(\theta/2)R_{ms}/9 \tag{2}$$

where Ma is the solar wind Mach number and R_{ms} is the standoff distance of the magnetopause.

Weimer (2001) described an improved model of the ionospheric electric potentials, in which the IMF magnitude and solar wind velocity have been replaced by solar wind electric field and dynamic pressure. The solar wind electric field is multiplied by a factor of $B^{-1/3}$ to account for nonlinear changes in the effective width of the solar wind coupling region. Kivelson and Ridley (2008) derived the dependence of the CPCP on solar wind and ionospheric properties and proposed a CPCP formula that included the quasi-viscous term from Boyle et al. (1997), and their CPCP equation is

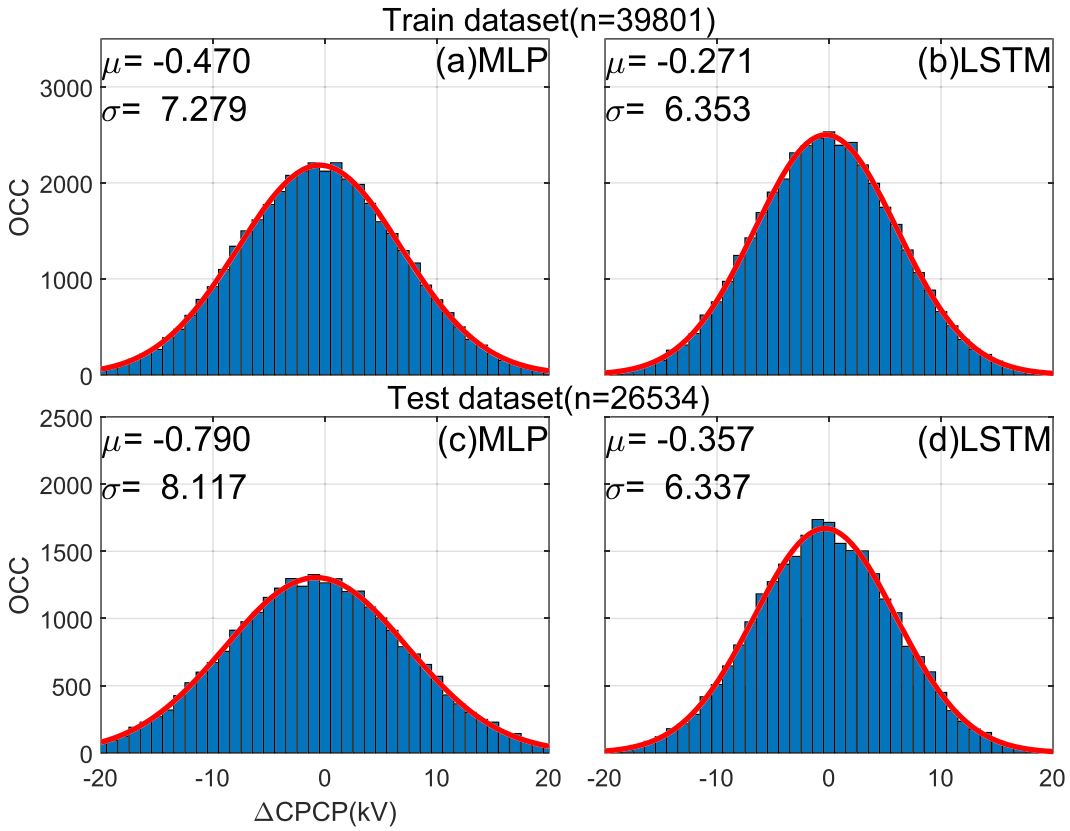

Figure 7. The error histograms of the CPCP between the measurements from SuperDARN and the predicted values from deep learning models. The (a) MLP model and (b) LSTM model using the training data set. The (c) MLP model and (d) LSTM model using the testing data set. The red solid curves are Gaussian best fitting calculations with the mean (μ) and variance (σ) values on the upper left corner.

$$\mathrm{CPCP} = \left(10^{-4}v^2 + 0.2\pi E_r R_{ms}\frac{1}{1+\mu_0 v_A \sum p}\right) \tag{3}$$

where v_A is the upstream Alfven speed and $\sum p$ is the height-integrated Pederson conductance of the ionosphere. Another interesting work has been reported by Bristow et al. (2004), who examined the SuperDARN data statistically and obtained a best fit linear model for the potential as a function of the solar wind and IMF as follows:

$$\mathrm{CPCP} = a + bvB\sin^3(\theta/2) \tag{4}$$

where a and b are the coefficients determined by a best fit to the selected data. The accuracy of the models can be checked and compared with other models by a Taylor diagram (Taylor, 2001). The Taylor diagram contains three performance parameters (RMSE, standard deviation [STD], and LC) in one figure and can present the results of different models simultaneously by showing them with different markers. Figure 9 is a Taylor diagram for comparison of the deep learning models developed here with previous models based on the testing data set in this study. The green, blue, and black axes stand for RMSE, LC, and STD, respectively. The red round dot is the location of measurements from SuperDARN based on TS18. The red arc represents the measured STD, which is about 18.51 kV. For direct comparison, we applied the equation of Boyle et al. (1997) (denoted as "Boy"), the expression of Bristow et al. (2004) (denoted as "Bri"), and the equation of Ridley (2005) (denoted as "Rid") to the solar wind conditions measured during the periods used in this study. In addition, a multivariate linear regression (MLR) analysis is performed for further comparison. The result from RG96 is also included in this Taylor diagram. It was revealed that the MLP and LSTM outcomes are better such that the correlation coefficients are approximately 0.84 and

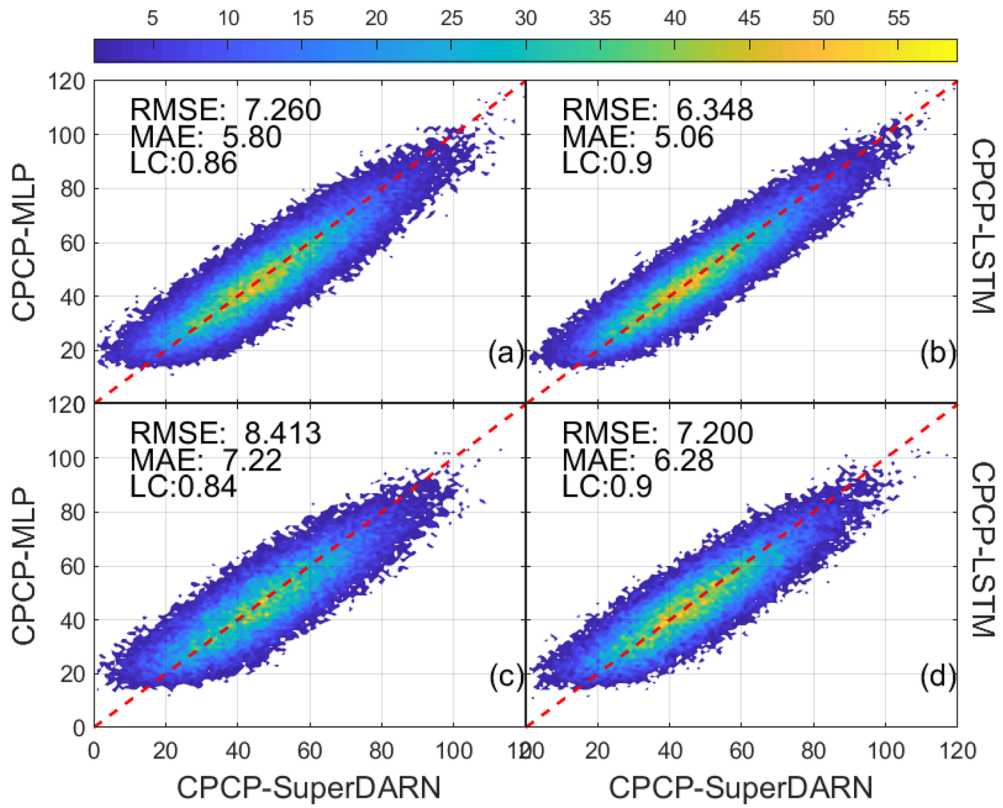

Figure 8. Comparison between measured CPCP and predictions. (a and b) For training data and (c and d) for testing data. The red dashed line represents the ideal case when the prediction is equal to the measured CPCP. The contours of the data occurrence are also plotted.

0.90, respectively, considerably higher than 0.72 for Bri and 0.74 from MLR or 0.71 from Boy and 0.69 from Rid. It is also interesting to note that the RMSE values for the MLP and LSTM models are 8.41 and 7.20 kV, which are noticeably lower than for the other four models. The deep learning models have bigger correlation coefficients and smaller RMSE values than have the other models. In addition, the Bri and MLR models stand out as the better prediction methods for lower STD than do the Boy and Rid models, which can be expected because the latter equations are derived from satellite data, which generally estimate higher CPCP values than does SuperDARN (Koustov et al., 2019; Xu et al., 2008), thus partially leading to a larger STD and RMSE. Additionally, due to the mathematical nature of the multivariate regression method, the MLR and Bri models have smaller STDs of 9.92 and 12.15 kV compared to the measured 15.94 kV STD from RG96 and 18.51 kV STD from TS18. The STD values from the deep learning techniques are closer to the STD values of the measurements than are those from the other models, which means that the deep learning models do a better job of estimating the variability of the CPCP than do the other models. Also, a very interesting feature that is noteworthy here is that the models can be grouped into three types according to the STD in the Taylor diagram, namely, Bri and MLR models, deep learning models, and Boy and Rid models. This is because the Bri and MLR models are both based on MLR analysis, the deep learning models are based on nonlinear regression, and the Boy and Rid models are mainly from the same fixed formula. Figure 9 summarizes the finding that the proposed deep learning models provide a remarkable improvement in overall performance such that models may be ranked in order as LSTM, MLP, MLR, Bri, Rid, and Boy in terms of predictive quality for the data set under consideration. We also note here that the LSTM model gives the better prediction performance considering the 8-min history values of near-Earth parameters, which is a little smaller than the response time of the high-latitude ionospheric convection to IMF changes reported in some past literature (Nishitani et al., 2002). After that, the performance no longer improves clearly, which probably means that the 8-min history values may contribute the most important part of

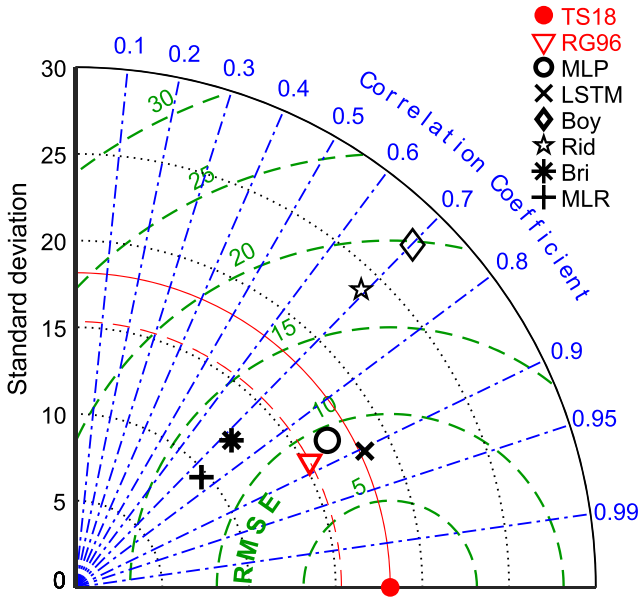

Figure 9. Taylor diagram for comparison of several models, which are from SuperDARN measurements (red round dot, "TS18"), deep learning models (circle for "MLP" and multiplication sign for "LSTM"), Boyle et al. (1997) (diamond, "Boy"), Bristow et al. (2004) (star, "Bri"), Ridley (2005) (asterisk, "Rid"), multivariate linear regression model (plus sign, "MLR"), and RG96.

the effect of the coupled energy on the ionospheric plasma convection. It is also clear from the above discussion that there are a number of factors that could be taken into account when developing CPCP models, that is, diurnal, seasonal, solar activity factors and the uncertainties from the algorithm itself when computing the best fit global solution of the electrostatic potential and limiting the low-latitude zero potential boundary of the convection zone. However, considering all these factors when applying deep learning would lead to many additional complications. A more suitable selection criterion for the deep learning input remains crucial in the future.

For the validation of a CPCP prediction model, error analysis alone is not enough. Therefore, we examine the prediction ability of our deep learning models by plotting the CPCP values versus IEF, Ekl, and the *AE* index in Figure 10. The red, blue, and green lines are for SuperDARN measurements, the MLP model, and the LSTM model, respectively. The CPCP values have been averaged by IEF and Ekl bins of 1 mV/m and *AE* bins of 100. The corresponding STD bars are also presented. The variations of CPCP from the MLP and LSTM models with IEF, Ekl, and the *AE* index agree very well with measurements from SuperDARN. In Figure 10a, the mean value curves become nonlinear starting from about 3 to 4 mV/m, which is reasonably consistent with studies of saturation effects reported by others, such as Koustov et al. (2009). The deep learning algorithms express the nonlinear trend quite well. Almost the same features can be found in Figures 10b and 10c. This further demonstrates the excellent prediction ability using deep learning methods.

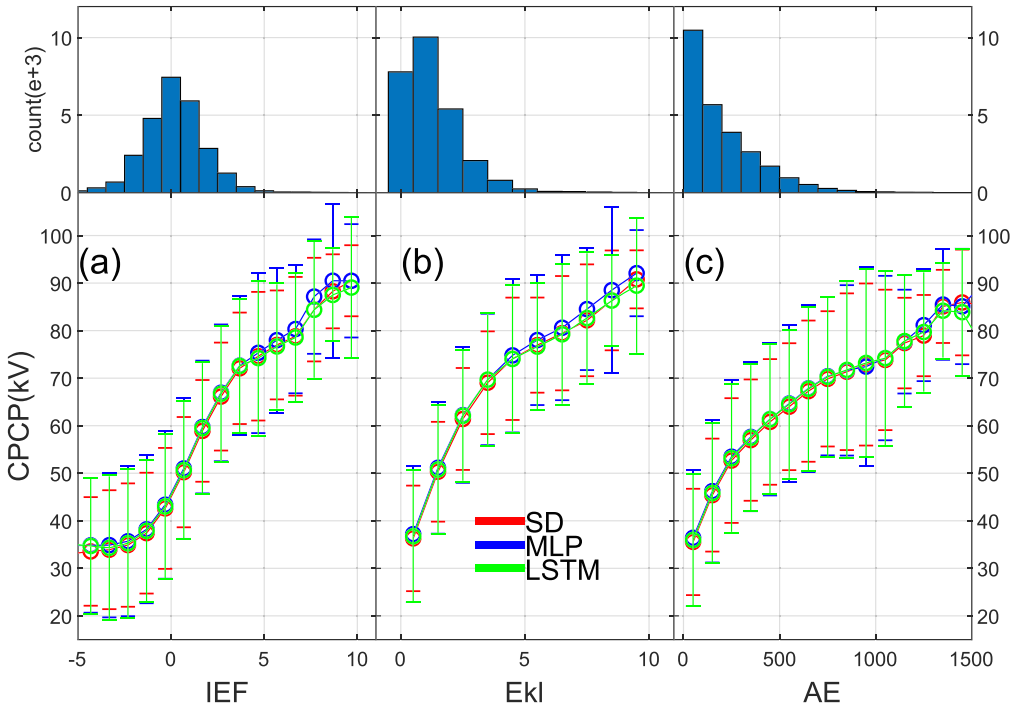

Figure 10. CPCP variations versus the (a) interplanetary electric field (IEF), (b) Kan-Lee merging electric field (Ekl), and (c) the *AE* index. The red, blue, and green lines are for SuperDARN measurement, the MLP model, and the LSTM model, respectively. The CPCP values have been averaged by IEF and Ekl bins of 1 mV/m and *AE* bins of 100. The corresponding standard deviation bars are also presented.

Although the SuperDARN CPCPs reported here are generally consistent with previous studies (Koustov et al., 2009; Shepherd et al., 2003), we acknowledge that the CPCP values estimated using satellite-based equipment or by some models (Hairston et al., 2003; Khachikjan et al., 2008) are generally higher, a discrepancy that has not been entirely resolved. So further validation work on the SuperDARN CPCP is necessary. However, each technique or model has limitations on the degree and accuracy to which it can determine or predict CPCP. Comparing to other measurements, the advantages using SuperDARN are that the radars operate continuously and provide substantial spatial coverage from the midlatitude to the polar cap ionosphere. The SuperDARN potential measurements can also benefit from a wide spatial distribution of measurements and a fine temporal resolution, typically 1 or 2 min, which is very useful for exploring potential variations over short time periods. For the CPCP determination based on satellites, a convection pattern can only be obtained on time scales of 100 min or longer, and there is no guarantee that the satellite's trajectory will cross through the exact location of the potential pattern's minimum and maximum.

5. Conclusions

In this research, we first correlated the CPCP with candidate solar wind, magnetopause, and geomagnetic parameters, and three parameters, IEF, Ekl and the *AE* index, were selected to be the vectors. Next, two deep learning models for SuperDARN CPCP were proposed. We tested these two models with an independent data set, and the achieved results show that the RMSE, MAE, and LC are 8.41 kV, 7.22 kV, and 0.84 for MLP and 7.20 kV, 6.28 kV, and 0.90 for LSTM, respectively, which are much better than those from the other models. Using MLP and LSTM for deep learning to build the CPCP prediction models is an innovative approach. CPCP prediction has been improved owing to the correlation coefficients calculation and by taking advantage of historical values. The proposed models are effective in raising the prediction accuracy and reducing the prediction error of the CPCP. In addition, comparison with other models based on the same data set demonstrates that this approach is helpful for estimating the CPCP. We plan additional research on the construction of instantaneous ionospheric electric potential patterns based on deep learning in the near future.

Acknowledgments

This work was supported in part by the National Key R&D Program of China (2018YFC1407300 and 2018YFC1407304), in part by the National Natural Science Foundation of China (Grants 41704154, 41431072, and 41674169) and in part by Opening Fund of SOA Key Laboratory for Polar Science (Grant KP201503). The authors acknowledge the use of SuperDARN data (URL: http://vt.superdarn.org/tiki-index.php?page=ASCIIData), which are freely available through the SuperDARN website at Virginia Polytechnic Institute and State University (URL: http://vt.superdarn.org/). SuperDARN is a collection of radars funded by the national scientific funding agencies of Australia, Canada, China, France, Italy, Japan, Norway, South Africa, the United Kingdom, and the United States of America. We also acknowledge the use of NASA/GSFC's Space Physics Data Facility's OMNI Web service and OMNI data (URL: https://omniweb.gsfc.nasa.gov/ow.html). We thank Professor John Michael Ruohoniemi at Virginia Tech for the fruitful discussions and comments on this research.

References

Adhikari, B., Baruwal, P., & Chapagain, N. P. (2017). Analysis of supersubstorm events with reference to polar cap potential and polar cap index. *Earth and Space Science*, *4*(1), 2–15.

Axford, W. I., & Hines, C. O. (1961). A unifying theory of high-latitude geophysical phenomena and geomagnetic storms. *Canadian Journal of Physics*, *39*(10), 1433–1464.

Borda, R. A. F., Mininni, P. D., Mandrini, C. H., Gómez, D. O., Bauer, O. H., & Rovira, M. G. (2002). Automatic solar flare detection using neural network techniques. *Solar Physics*, *206*(2), 347–357.

Boyle, C., Reiff, P., & Hairston, M. (1997). Empirical polar cap potentials. *Journal of Geophysical Research*, *102*(A1), 111–125.

Bristow, W. A., Greenwald, R. A., Shepherd, S. G., & Hughes, J. M. (2004). On the observed variability of the cross-polar cap potential. *Journal of Geophysical Research*, *109*, A02203. https://doi.org/10.1029/2003JA010206

Chisham, G., Lester, M., Milan, S. E., Freeman, M. P., Bristow, W. A., Grocott, A., et al. (2007). A decade of the Super Dual Auroral Radar Network (SuperDARN): Scientific achievements, new techniques and future directions. *Surveys in Geophysics*, *28*(1), 33–109.

Clauer, C. R., Xu, Z., Maimaiti, M., Ruohoniemi, J. M., Scales, W., Hartinger, M. D., et al. (2016). Investigation of a rare event where the polar ionospheric reverse convection potential does not saturate during a period of extreme northward IMF solar wind driving. *Journal of Geophysical Research: Space Physics*, *121*, 5422–5435. https://doi.org/10.1002/2016JA022557

Cowley, S., & Lockwood, M. (1992). Excitation and decay of solar wind-driven flows in the magnetosphere-ionosphere system. *Annales Geophysicae*, *10*, 103–115.

Doyle, M. A., & Burke, W. J. (1983). S3-2 measurements of the polar cap potential. *Journal of Geophysical Research*, *88*(A11), 9125–9133.

Dungey, J. W. (1961). Interplanetary magnetic field and the auroral zones. *Physical Review Letters*, *6*(2), 47.

Förster, M., & Haaland, S. (2015). Interhemispheric differences in ionospheric convection: Cluster EDI observations revisited. *Journal of Geophysical Research: Space Physics*, *120*, 5805–5823.

Gillies, D. M., Mcwilliams, K. A., Maurice, J. P. S., & Milan, S. E. (2011). Global-scale observations of ionospheric convection during geomagnetic storms. *Journal of Geophysical Research*, *116*, A12238. https://doi.org/10.1029/2011JA017086

Graves, A. (2012). Supervised sequence labelling. In *Supervised sequence labelling with recurrent neural networks* (pp. 5–13). Berlin, Heidelberg: Springer.

Grocott, A., Laurens, H. J., & Wild, J. A. (2017). Nightside ionospheric convection asymmetries during the early substorm expansion phase: Relationship to onset local time. *Geophysical Research Letters*, *44*, 11,696–11,705. https://doi.org/10.1002/2017GL075763

Hairston, M. R., Drake, K. A., & Skoug, R. (2005). Saturation of the ionospheric polar cap potential during the October–November 2003 superstorms. *Journal of Geophysical Research*, *110*, A09S26. https://doi.org/10.1029/2004JA010864

Hairston, M. R., Hill, T. W., & Heelis, R. A. (2003). Observed saturation of the ionospheric polar cap potential during the 31 March 2001 storm. *Geophysical Research Letters*, *30*(6), 1325. https://doi.org/10.1029/2002GL015894

Hoff, J., Townsend, L., & Hines, J. (2003). Prediction of energetic solar particle event dose-time profiles using artificial neural networks. *IEEE Transactions on Nuclear Science*, *50*(6), 2296–2300.

Huang, D., Liu, E., Hu, H., & Liu, J. (2018). Algorithm for the estimation of ionosphere parameters from ground scatter echoes of SuperDARN. *SCIENCE CHINA Technological Sciences*, *61*(11), 1755–1764. https://doi.org/10.1007/s11431-017-9178-4

Kan, J. R., & Lee, L. C. (1979). Energy coupling function and solar wind-magnetosphere dynamo. *Geophysical Research Letters*, *6*(7), 577–580.

Khachikjan, G. Y., Koustov, A., & Sofko, G. (2008). Dependence of SuperDARN cross polar cap potential upon the solar wind electric field and magnetopause subsolar distance. *Journal of Geophysical Research*, *113*, A09214. https://doi.org/10.1029/2008JA013107

Kivelson, M. G., & Ridley, A. J. (2008). Saturation of the polar cap potential: Inference from Alfvén wing arguments. *Journal of Geophysical Research*, *113*, A05214. https://doi.org/10.1029/2007JA012302

Koustov, A., Lavoie, D., Kouznetsov, A., Burchill, J., Knudsen, D., & Fiori, R. (2019). A comparison of cross-track ion drift measured by the Swarm satellites and plasma convection velocity measured by SuperDARN. *Journal of Geophysical Research: Space Physics*, *124*, 4710–4724. https://doi.org/10.1029/2018JA026245

Koustov, A. V., Khachikjan, G. Y., Makarevich, R. A., & Bryant, C. (2009). On the SuperDARN cross polar cap potential saturation effect. *Annales Geophysicae*, *27*(10), 3755–3764.

Kustov, A. V., Papitashvili, V. O., Sofko, G. J., Schiffler, A., Feldstein, Y. I., Gromova, L. I., et al. (1997). Dayside ionospheric plasma convection, electric fields, and field-aligned currents derived from the SuperDARN radar observations and predicted by the IZMEM model. *Journal of Geophysical Research*, *102*(A11), 24,057–24,067.

Liemohn, M., & Ridley, A. (2002). Comment on "Nonlinear response of the polar ionosphere to large values of the interplanetary electric field" by CT Russell et al. *Journal of Geophysical Research*, *107*(A12), 1460. https://doi.org/10.1029/2002JA009440

Lin, J.-W., Chao, C.-T., & Chiou, J.-S. (2018). Determining neuronal number in each hidden layer using earthquake catalogues as training data in training an embedded back propagation neural network for predicting earthquake magnitude. *IEEE Access*, *6*, 52,582–52,597.

Liu, E., Hu, H., Liu, J., Teng, X., & Qiao, L. (2019). Predicting SuperDARN cross polar cap potential by applying regression analysis and machine learning. *Journal of Atmospheric and Solar-Terrestrial Physics*, *193*, 105,057.

Mori, D., & Koustov, A. V. (2013). SuperDARN cross polar cap potential dependence on the solar wind conditions and comparisons with models. *Advances in Space Research*, *52*(6), 1155–1167. https://doi.org/10.1016/j.asr.2013.06.019

Nishitani, N., Ogawa, T., Sato, N., Yamagishi, H., Pinnock, M., Villain, J. P., et al. (2002). A study of the dusk convection cell's response to an IMF southward turning. *Journal of Geophysical Research*, *107*(A3), 1036. https://doi.org/10.1029/2001JA900095

Nishitani, N., Ruohoniemi, J. M., Lester, M., Baker, J., Koustov, A. V., Shepherd, S., et al. (2019). Review of the accomplishments of mid-latitude Super Dual Auroral Radar Network (SuperDARN) HF radars. *Progress in Earth and Planetary Science*, *6*(1), 57.

Reiff, P. H., Spiro, R. W., & Hill, T. W. (1981). Dependence of polar cap potential drop on interplanetary parameters. *Journal of Geophysical Research*, *86*(A9), 7639–7648.

Ridley, A. (2005). A new formulation for the ionospheric cross polar cap potential including saturation effects. *Annales Geophysicae*, *23*, 15.

Ridley, A., Crowley, G., & Freitas, C. (2000). An empirical model of the ionospheric electric potential. *Geophysical Research Letters*, *27*(22), 3675–3678.

Ruohoniemi, J. M., & Baker, K. B. (1998). Large-scale imaging of high-latitude convection with Super Dual Auroral Radar Network HF radar observations. *Journal of Geophysical Research*, *103*(A9).

Ruohoniemi, J. M., & Greenwald, R. A. (1996). Statistical patterns of high-latitude convection obtained from Goose Bay HF radar observations. *Journal of Geophysical Research*, *101*(A10), 21,743–21,721.

Ruohoniemi, J. M., & Greenwald, R. A. (2005). Dependencies of high-latitude plasma convection: Consideration of interplanetary magnetic field, seasonal, and universal time factors in statistical patterns. *Journal of Geophysical Research*, *110*, A09204. https://doi.org/10.1029/2004JA010815

Russell, C., Luhmann, J., & Lu, G. (2001). Nonlinear response of the polar ionosphere to large values of the interplanetary electric field. *Journal of Geophysical Research*, *106*(A9), 18,495–18,504.

Shepherd, S., & Ruohoniemi, J. (2000). Electrostatic potential patterns in the high-latitude ionosphere constrained by SuperDARN measurements. *Journal of Geophysical Research*, *105*(A10), 23,005–23,014.

Shepherd, S. G. (2007). Polar cap potential saturation: Observations, theory, and modeling. *Journal of Atmospheric and Solar-Terrestrial Physics*, *69*(3), 234–248.

Shepherd, S. G., Greenwald, R. A., & Ruohoniemi, J. M. (2002). Cross polar cap potentials measured with Super Dual Auroral Radar Network during quasi-steady solar wind and interplanetary magnetic field conditions. *Journal of Geophysical Research*, *107*(A7), 1094. https://doi.org/10.1029/2001JA000152

Shepherd, S. G., Ruohoniemi, J. M., & Greenwald, R. A. (2003). Testing the Hill model of transpolar potential with Super Dual Auroral Radar Network observations. *Geophysical Research Letters*, *30*(1), 1002. https://doi.org/10.1029/2002GL015426

Sun, W., Xu, L., Huang, X., Zhang, W., Yuan, T., Chen, Z., & Yan, Y. (2017). *Forecasting of ionospheric vertical total electron content (TEC) using LSTM networks*. Paper presented at 2017 International Conference on Machine Learning and Cybernetics (ICMLC), Ningbo, China.

Tan, Y., Hu, Q., Wang, Z., & Zhong, Q. (2018). Geomagnetic index *Kp* forecasting with LSTM. *Space Weather—The International Journal of Research & Applications*, *16*(4).

Taylor, K. E. (2001). Summarizing multiple aspects of model performance in a single diagram. *Journal of Geophysical Research*, *106*(D7), 7183–7192.

Thomas, E. G., & Shepherd, S. G. (2018). Statistical patterns of ionospheric convection derived from mid-latitude, high-latitude, and polar SuperDARN HF radar observations. *Journal of Geophysical Research: Space Physics*, *123*, 3196–3216. https://doi.org/10.1002/2018JA025280

Valach, F., Revallo, M., Bochníček, J., & Hejda, P. (2009). Solar energetic particle flux enhancement as a predictor of geomagnetic activity in a neural network-based model. *Space Weather*, *7*(4).

Wang, G. (2016). A perspective on deep imaging. *IEEE Access*, *4*, 8914–8924.

Weimer, D. (1996). A flexible, IMF dependent model of high-latitude electric potentials having "space weather" applications. *Geophysical Research Letters*, *23*(18), 2549–2552.

Weimer, D. (2001). An improved model of ionospheric electric potentials including substorm perturbations and application to the Geospace Environment Modeling November 24, 1996, event. *Journal of Geophysical Research*, *106*(A1), 407–416.

Weimer, D. (2005). Improved ionospheric electrodynamic models and application to calculating Joule heating rates. *Journal of Geophysical Research*, *110*, A05306. https://doi.org/10.1029/2004JA010884

Wilder, F. D., Clauer, C. R., Baker, J. B. H., Cousins, E. P., & Hairston, M. R. (2011). The nonlinear response of the polar cap potential under southward IMF: A statistical view. *Journal of Geophysical Research*, *116*, A12229. https://doi.org/10.1029/2011JA016924

Wintoft, P., & Lundstedt, H. (1999). A neural network study of the mapping from solar magnetic fields to the daily average solar wind velocity. *Journal of Geophysical Research*, *104*(A4), 6729–6736.

Xu, L., Koustov, A. V., Xu, J. S., Drayton, R. A., & Huo, L. (2008). A 2-D comparison of ionospheric convection derived from SuperDARN and DMSP measurements. *Advances in Space Research*, *42*(7), 1259–1266.

Yang, L., Zheng, Y., Cai, X., Dai, H., Mu, D., Guo, L., & Dai, T. (2018). A LSTM based model for personalized context-aware citation recommendation. *IEEE access*, *6*, 59,618–59,627.

Yang, Y., Shen, F., Yang, Z., & Feng, X. (2018). Prediction of solar wind speed at 1 AU using an artificial neural network. *Space Weather*, *16*. https://doi.org/10.1029/2018SW001955

Zhang, S.-R., Holt, J. M., & McCready, M. (2007). High latitude convection based on long-term incoherent scatter radar observations in North America. *Journal of Atmospheric and Solar-Terrestrial Physics*, *69*(10–11), 1273–1291.